

We are IntechOpen, the world's leading publisher of Open Access books Built by scientists, for scientists

4,400

Open access books available

117,000

International authors and editors

130M

Downloads

Our authors are among the

154

Countries delivered to

TOP 1%

most cited scientists

12.2%

Contributors from top 500 universities



WEB OF SCIENCE™

Selection of our books indexed in the Book Citation Index
in Web of Science™ Core Collection (BKCI)

Interested in publishing with us?
Contact book.department@intechopen.com

Numbers displayed above are based on latest data collected.
For more information visit www.intechopen.com



Research on Shape Memory Alloys and Magnetorheological Fluids for Use in Pneumatic Actuators

*Edmundas Kibirškis, Darius Pauliukaitis
and Kęstutis Vaitasius*

Abstract

Adaptive vibrating actuators operating under autovibration regime were developed using materials with shape memory (SM). Mechanical characteristics of such type vibroactuators can be adjusted by changing geometrical parameters of chamber or throttle. It allows to expand the application of pneumatic vibroexciters and use them in different technological processes. Pneumatic vibroactuator elements that consist of magnetorheological (MR) fluids are proposed for micro-throttle and microcompressor design. The main properties of used MR materials and theoretical background of their mechanical and physical parameters are presented, some results of experimental and theoretical research of actuators are introduced and conclusions of the performed research are formulated.

Keywords: pneumatic actuator, magnetorheological fluid, microcompressor, micro choke, shape memory element

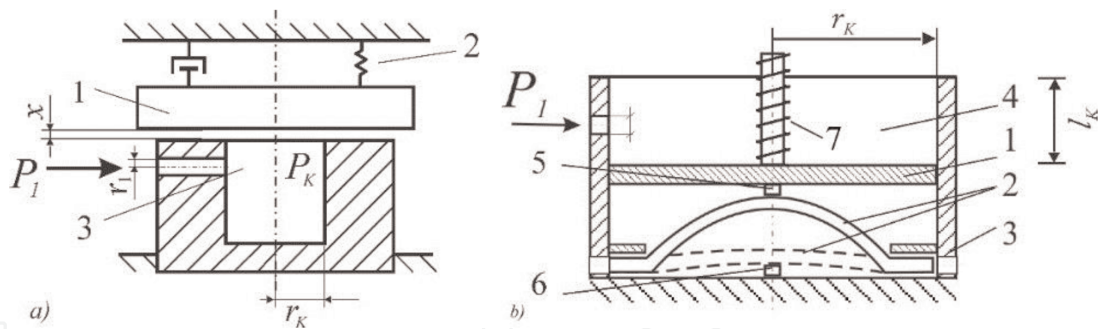
1. Introduction

Smart materials can be used in various technologies, including the structures of pneumatic actuators on air cushions. These actuators may be applied in different technological devices: in vehicle suspensions, rotary mechanisms, vibrating damping systems, various medical devices, etc. Some properties of actuators with elements of shape memory alloy and magnetorheological fluid are analysed in this study.

2. Theoretical background of the use of materials containing shape memory elements in pneumatic actuators

Functional capabilities of pneumatic actuators [1] can be extended via the variations of their ignition chamber volume or the geometrical parameters of their choke [2].

The structure of any pneumatic actuator containing a shape memory (SM) element, i.e. a variable volume chamber, is provided in **Figure 1**. Such transducers may be used in vibratory machinery, pneumatic shock-absorber structures and regulatory, guidance, positioning and other equipment.


Figure 1.

Schemes of pneumatic vibroexciters constructions, (a) simplified scheme of vibrodrive: 1—oscillatory mass; 2—spring; 3—exciting chamber of vibrodrive; P_1 —supplied gas pressure; P_K —pressure inside chamber; x —move of oscillatory mass; r_1 —radius of the air supply channel; and r_K —chamber radius. (b) Simplified scheme with element made from smart material: 1—piston; 2—arc-shaped plate with SM material; 3—frame, 4—exciting chamber; 5,6—cooling and heating elements, respectively; 7—spring that pushes piston 1 to the plate 2; r_K —exciting chamber radius; and l_K —chamber height.

Any ignition chamber of a pneumatic actuator consists of transmission (**Figure 1b**), which is made of plunger 1, SM arch element 2, cooler 5 and heating elements 6. SM transmission element 2 is situated in case 3. Transmission 2 contacts heating 6 and cooling 5 elements. Its plate 2 is being heated, and the heat is being transmitted to the arch element. When the arch material reaches the reverse martensitic transformation temperature, it begins to incline in the opposite direction, and when it reaches the opposite position, the system starts cooling. When the arch material reaches temperature which is lower than its phase transformation temperature, the arch escapes to the backwards direction.

By experimental study of shape memory alloys, it was found that temperature range is about 10–16°C when direct and reverse martensitic transformation happens with SM material (NiTi alloy). So, it is important to mention, in a separate case, the system shown in **Figure 1b** without complex feedback control elements 5 and 6.

Based on previous research works [3–5], the plate containing the SM material (nickel and titanium alloy) has been researched as a uniform plate without its decomposition into the core and the outer layer although they could be described as having different deformation properties. Those works offered simplified methods for the calculation of deformations in plates containing SM material. Suppose the plate is situated on a horizontal axis and one or both of its ends are fixed. Its centre is being affected by force which is directed along vertical axis. If the effect of transverse forces that appear during the deformation is ignored, a homogenous bending of the plate in the direction of Y axis can be described using the equation of Euler:

$$EJ \frac{d^2 y}{dx^2} + Py \left[1 + \left(\frac{dy}{dx} \right)^2 \right]^{\frac{3}{2}} = 0 \quad (1)$$

where E refers to the Young's modulus, J refers to inertia moment and P refers to force which affects the centre of the plate. If both ends of the sample are fixed, marginal conditions of Eq. (1) will be as follows:

$$y(0) = y(l) = 0 \quad (2)$$

where l refers to the plate length.

Properties of SM material used are presented in **Table 1**.

The number of experiments led to drawing the curve which shows the correlation between mechanical stress with temperatures in nickel and titanium alloy plate

(Figure 2). Based on theoretical assumptions contained in the mentioned works [3, 7–17], such calculations can be also used in chains containing SM elements. While heating the plate up to the austenitic temperature, the sinusoidal bending will be obtained:

$$a \sin \frac{\pi \xi}{l} \quad (3)$$

where a refers to the maximum bending of the plate.

Taking into account Eq. (1), the close solution of bending in the direction of Y axis in the sample whose both ends are fixed can be found [3, 7]:

$$y(\xi) = \frac{2^{\frac{3}{2}} l}{\pi} \sqrt{\frac{\sigma - \sigma_1}{\sigma_1}} \sin \frac{\pi \xi}{l} + o(\sqrt{\sigma - \sigma_1}) \quad (4)$$

where the minimum marginal stress is described as

$$\sigma_1 = \frac{\pi^2 E J}{l^2 S} \quad (5)$$

Martensite start temperature, M_s	18.4°C
Martensite finish temperature, M_f	9°C
Austenite start temperature, A_s	34.5°C
Austenite finish temperature, A_f	49°C
Transformation constant, C_M	0.008 GPa/°C
Transformation constant, C_A	0.0138 GPa/°C
Transformation constant, σ_s^{cr}	0.1 GPa
Transformation constant, σ_f^{cr}	0.17 GPa

Table 1.
 Properties of NiTi material [6].

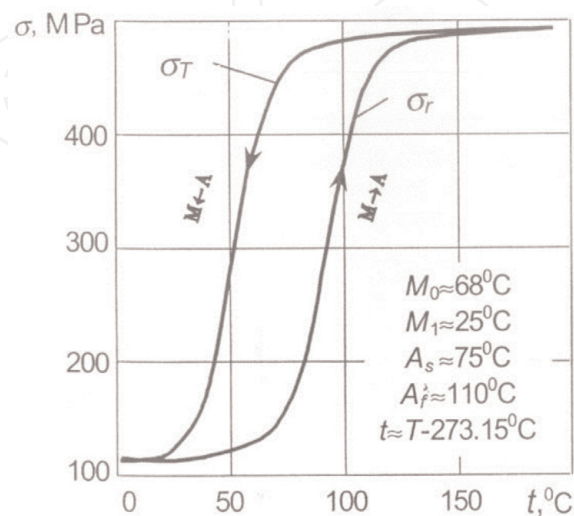


Figure 2.
 Correlation between mechanical stress and temperature in nickel and titanium alloy plate: σ_r —reaction stress; σ_T —martensitic transformation stress; M_0 and M_1 —direct martensitic transformation ($A \rightarrow M$) temperatures, initial and terminal, respectively; and A_0 and A_1 —reverse martensitic transformation ($M \rightarrow A$) temperatures, initial and terminal, respectively [3].

and the arched axis is described by a sinusoid

$$y(\xi) = \frac{2^{\frac{3}{2}}l}{\pi} \sqrt{\frac{\sigma - \sigma_1}{\sigma_1}} \sin \frac{\pi\xi}{l} \quad (6)$$

while inertia moment of the plate section in regard to neutral axis is equal to

$$J = \frac{bh^3}{12} \quad (7)$$

If $S = bh$ is the plate section area (**Figure 3**), E is an elasticity module of nickel and titanium alloy (app $E = 15.65 \times 10^{10}$ Pa).

The force acting upon the plate with SM effect can be defined by the formula

$$F = \begin{cases} SE_{ad}\alpha(T - T_0), & \text{when } T_0 \leq T < A_0 \\ S\sigma_r, & \text{when } A_0 \leq T < A_1 \\ SE_{ad}\alpha(T - A_1), & \text{when } T > A_1 \end{cases} \quad (8)$$

where T , α and E_{ad} are temperature, thermal expansion coefficient and adiabatic Young's modulus, respectively. By Eqs. (5) and (8), the smallest critical force, when temperature changes between initial and final reverse martensitic transformation temperatures ($A_0 < T < A_1$), will have the following expression:

$$F_1 = \frac{\pi^2 EJ}{l^2} \quad (9)$$

When the temperature varies between A_0 and A_1 , the plate regains its present sinusoidal shape. When the temperature approaches critical temperature T_K , corresponding critical stress σ_K , the plate acquires the linear shape.

Pneumatical vibroexciter with exciting chamber radius $r_K = 15 \times 10^{-3}$ m and height $l_K = 20 \times 10^{-3}$ m has been analysed in the numerical research. A smart material element in exciting chamber has used a titanium-nickel plate whose length $l = 25 \times 10^{-3}$ m, height $h = 1.5 \times 10^{-3}$ m and width $b = 20 \times 10^{-3}$ m. By the experimental study [3], approximate Young's modulus for NiTi alloy is $E = 15.65 \times 10^{10}$ Pa, initial and final, respectively, reverse martensitic transformation temperatures $A_0 = 75^\circ\text{C}$ or $A_1 = 110^\circ\text{C}$.

According to Eqs. (3)–(9), a programme simulating the bending of plate has been proposed. The plate axis bending shapes in the direction of Y axis according to the plate length under the various reaction stresses σ_r are shown in **Figure 4a**.

The numerical researches have showed that a middle point of plate moves within 0.19×10^{-3} m in the direction of Y axis when the reaction stress is equal $\sigma_r = 463.4$ MPa. When the reaction stress is $\sigma_r = 464.0$ MPa, the maximum displacement of the plate middle point is about 0.91×10^{-3} m. According to the alloy

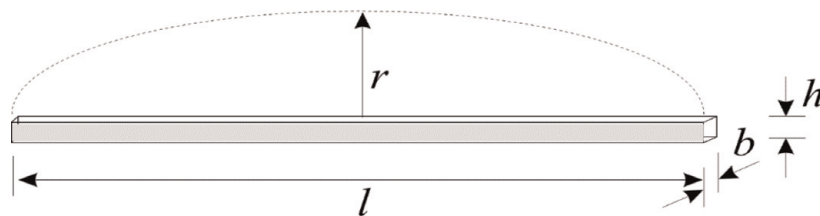


Figure 3.
Scheme of a nickel and titanium alloy plate.

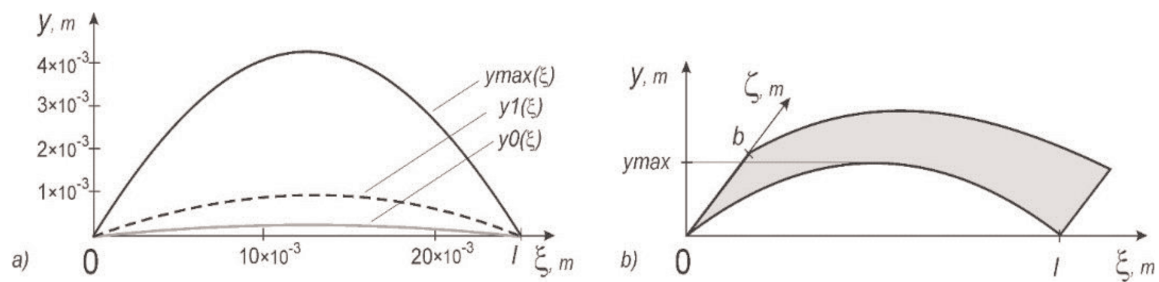


Figure 4. Deformation of the NiTi plate with the fastened ends: (a) shapes of bended plate under various stresses, curve $y_0(\xi)$, when $\sigma_r = 463.4$ MPa, the maximum deflection of bended plate is 0.19×10^{-3} m; curve $y_1(\xi)$ when $\sigma_r = 464.0$ MPa, the maximum deflection of bended plate is 0.91×10^{-3} m; and when curve $y_{max}(\xi)$ when $\sigma_r = 480.0$ MPa, the maximum deflection of bended plate is 4.26×10^{-3} m; (b) view of bended plate.

characteristics presented in the paper [3], the maximum stress could be $\sigma_r = 480.0$ MPa, and maximum deflection could reach the value 4.26×10^{-3} m. The critical stress was estimated to be $\sigma_K = 321$ MPa.

When stress exceeds critical stress (temperature varies between A_0 and A_1), the sample acquires a sinusoidal shape. It happens when stress exceeds critical margin:

$$\sigma > \left(1 + \frac{\pi^2 a^2}{2^3 l^2}\right) \sigma_K \quad (10)$$

Inequality (10) comes from Eqs. (3) and (4).

When temperature gets close to its critical margin t_K °C and the stress gets close to its critical level respectfully σ_K , bending of the sample decreases and obtains the shape of a line.

The area of the arched plate will be

$$S_B = \frac{L}{2} b \quad (11)$$

where L refers to the parameter of ellipse which is found having entered the complete elliptic interval of level 2 into Legendre form and e refers to elliptic eccentricity:

$$L = 4 \frac{l}{2} \int_0^{\frac{\pi}{2}} \sqrt{1 - e^2 \sin^2 \psi} d\psi \quad (12)$$

According to literature [4], linear deformations of the plate can be calculated

$$\varepsilon = \frac{S_B/2 - lb}{lb} \quad (13)$$

Having evaluated methods of identifying bending of the plate under various stresses (Eqs. (4)–(6)) and the deformations under the identified bending (Eqs. (11)–(13)), the authors have developed the software for calculating maximum bending values in plates containing SM materials when their critical stress is known, with additional capability of predicting the shape and the maximum force of bending in the plate. The obtained results are presented in **Figure 5**.

SM materials possess two rather distinctive properties: shape memory effect and superelasticity. Further, we will analyse a mathematical model aimed at the calculation of energy absorbed by the plate containing SM elements while it is being bent.

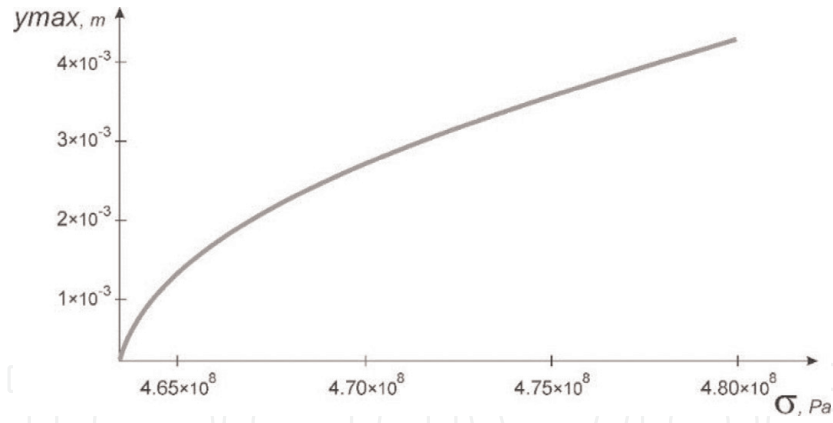


Figure 5. Dependence of deflection of NiTi plate with the fastened ends on the various reaction stresses.

Further on, we will identify the correlation between maximum bending of the sample and the force which affects it in heating and cooling phases. The overall deformation of the sample ε is equal to the sum of elastic deformation ε^e and phase transition deformation ε^{tr} :

$$\varepsilon = \varepsilon^e + \varepsilon^{tr} \quad (14)$$

According to the Bernoulli equation, the deformation can be expressed as follows [5]:

$$\varepsilon = \frac{2y}{L^2} (\delta_0 - \delta) \quad (15)$$

where δ_0 refers to initial bending and δ refers to bending after the effect of force F .

Elastic deformation ε^e can be expressed as

$$\varepsilon^e = \frac{\sigma}{E} \quad (16)$$

where σ refers to stress which occurs after the effect of force F , while E refers to Young's modulus.

The experiments [5] allowed identifying that deformation which occurs in the transition of phases which is directly proportional to martensitic fraction z_σ :

$$\varepsilon^{tr} = \gamma z_\sigma \quad (17)$$

where γ refers to maximum superelastic deformation.

The sum bending of the plate can be stated as follows:

$$\delta = \delta_0 + \delta_{SMA} + \delta_{EXT} \quad (18)$$

where δ_0 refers to initial bending, δ_{SMA} refers to bending which occurs in the transition of phases and δ_{EXT} refers to bending after the effect of force F .

Final expressions of bending for the process of heating and cooling are stated as follows:

$$\delta = \delta_0 + \frac{3a_2\gamma L^2}{2h} (T - A_f^1) + \frac{4L^3}{bEh^3} F \text{ (heating)} \quad (19)$$

$$\delta = \delta_0 + \frac{3a_2\gamma L^2}{2h} \left(T - M_f^0 - \frac{1}{a_2} \right) + \frac{4L^3}{bEh^3} F \text{ (cooling)} \quad (20)$$

where a_2 is a constant (measure unit K^{-1}), A_f^1 is temperature of terminating the austenitic phase and M_f^0 is temperature of terminating the martensitic phase.

Equations (19) and (20) make clear the existence of direct correlation between the temperature and the bending of the plate which describes its thermomechanical behaviour.

Eqs. (19) and (20) can be used for the calculation of bending in the plate containing SM elements and for the evaluation of minimum force which is necessary aiming to fix a certain shape of the plate. The numerical research has shown that force which is necessary for the counter-bending of plate varies from 370 to 135 N (it is equal to force being triggered by the plate), when temperature varies from 80 to 100°C.

Numerical results between the maximal displacement of middle point of bended plate and the various reaction stresses are shown in **Figure 5**.

Based on Eq. (6), it is possible to calculate restricted volume V_{PL} of bended plate Eq. (21) and find a changed capacity of exciting chamber:

$$V_{PL}(\sigma_r) = \int_0^b \int_0^l y(\sigma_r, \xi, \zeta) d\xi d\zeta \quad (21)$$

$$V_M = V_K - V_{PL}(\sigma_{\max}) \quad (22)$$

$$V_K = \pi r_K^2 l_K \quad (23)$$

The biggest volume of exciting chamber V_K when the plate has linear shape is expressed in Eq. (23). By using the above set of chamber and plate parameters, it has been found that volume of exciting chamber could be reduced from $V_K = 1.767 \times 10^{-5} \text{ m}^3$ to $V_M = 1.63 \times 10^{-5} \text{ m}^3$ (about 7.5%).

The volume of exciting chamber influence on vibrations of working body of vibroexciter is illustrated in **Figure 6**. During the numerical researches [18], after choosing particular geometrical parameters (r_{k1}, l_{k1}), initial tightening H_z , value of mass m_1 of working body of vibroexciter and amplitude of vibrations were $A_1 = 4.51 \times 10^{-3} \text{ m}$ and frequency $f_1 = 16.81 \text{ Hz}$ (autovibration shape X_1 in **Figure 6**). When the volume of chamber was reduced in 3%, the amplitude of vibrations decreased to a value $A_2 = 4.39 \times 10^{-3} \text{ m}$, and frequency increased to $f_2 = 16.92 \text{ Hz}$. When the volume of camera was reduced in 7.5%, amplitude of

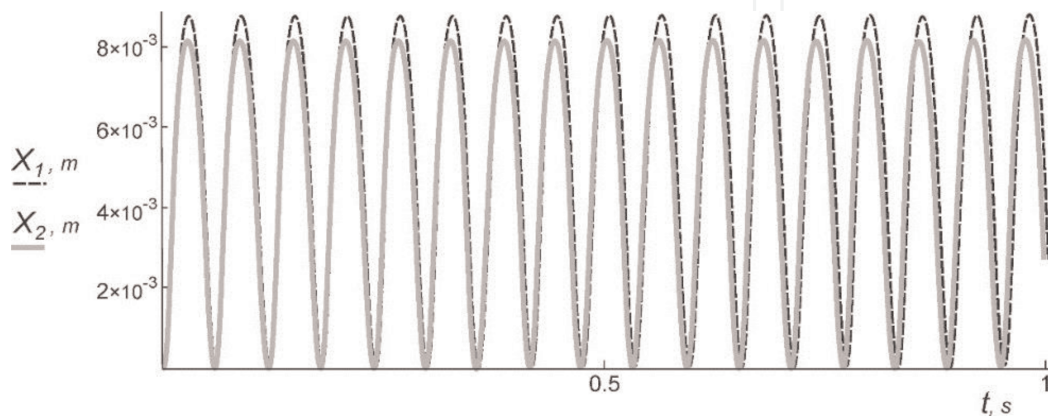


Figure 6. Autovibrations of mass 1 of vibroexciter in 1 s period: X_1 —without element with SMA; X_2 —when element with SMA works and decreases the volume of chamber in 7.5%.

vibrations become $A_3 = 4.10 \times 10^{-3}$ m and frequency heightened until $f_3 = 16.98$ Hz (autovibration shape X_2 in **Figure 6**).

2.1 Brinson's model

One dimensional composite mathematical model of internal variables has been offered by Brinson et al. [19, 20].

This model quantitatively evaluates the absorption of deformation energy and allows predicting marginal load which is necessary for the beginning and the termination of a martensitic phase transformation induced by stress [6, 19, 20]. There, martensitic fracture variable is being decomposed into two components depending on stress and temperature.

In this case, the distribution of deformation within the plate is not completely linear: material properties vary from martensitic to austenitic state along the thickness of the plate. While bending, there might be three stages of load defined. In the first stage, the SM sample is in austenitic stage along its thickness. In the second stage, when the load is being increased, the martensitic phase transformation, which is being induced by stress, starts in outer layers. Further increase of load provokes plastic deformations that are not included into the energy absorption calculation model [6, 21].

The deformation energy expression according to Brinson is as follows:

$$U = bL\sigma_0\varepsilon_0 \left[\frac{h_e}{6} + (h - h_e) \left(\frac{E_2}{2E_1} - 1 \right) + \left(1 - \frac{E_2}{E_1} \right) \frac{h^2 - h_e^2}{2h_e} + \frac{E_2 h^3 - h_e^3}{E_1 6h_e^2} \right], \quad (24)$$

while martensitic fraction, which is induced by stress, is stated as

$$\xi_S = \frac{1}{2} \cos \left\{ \frac{\pi}{\sigma_s^{cr} - \sigma_f^{cr}} \left[\sigma_0 \left(1 + \frac{E_2}{E_1} \left(\frac{2y}{h_e} - 1 \right) \right) \right] - \sigma_f^{cr} - C_M(T - M_S) \right\} + \frac{1}{2} \quad (25)$$

where σ_0 and ε_0 refer to stress and deformation, respectively, which call for the martensitic transformation; E_1 and E_2 refer to Young's modulus before and after martensitic phase transformation, which had been induced by stress, respectively; σ_s^{cr} and σ_f^{cr} refer to transformation constant; and h_e refers to the thickness of sample core in austenitic stage.

Brinson model evaluates the absorption of deformation energy in SM alloy in both superelasticity and martensitic stages. In addition, it defines the correlation between deformation energy and the thickness of SM plate core.

3. Magnetorheological fluids for use in pneumatic actuators

3.1 Theoretical and experimental background of the micro choke with magnetorheological fluid transmission

Some particularities of the application of magnetorheological (MR) fluid transmissions in microcompressors and pneumatic chokes had been described in scientific works [21–33].

Commonly, magnetorheological fluids are used in three flow modes, as shown in **Figure 7**. Magnetic poles are stationary, and MR fluid is flowing due to a pressure difference perpendicular to magnetic field in valve mode. In the case of shear mode, one of the magnetic poles is moving with respect to the other pole, and the MR fluid

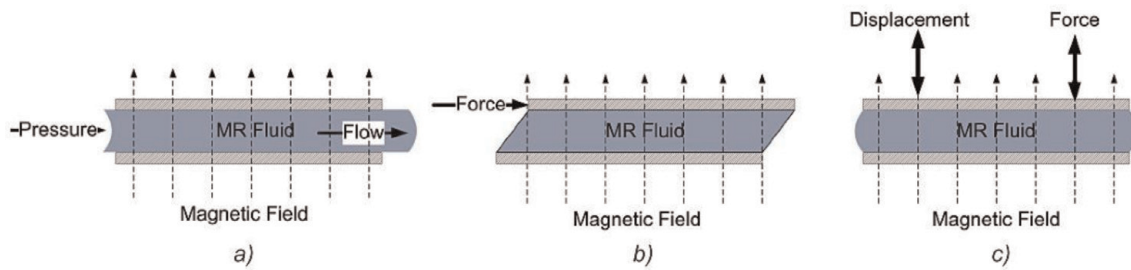


Figure 7.
 MR fluid flow modes: (a) valve mode, (b) shear mode, and (c) squeeze mode [31].

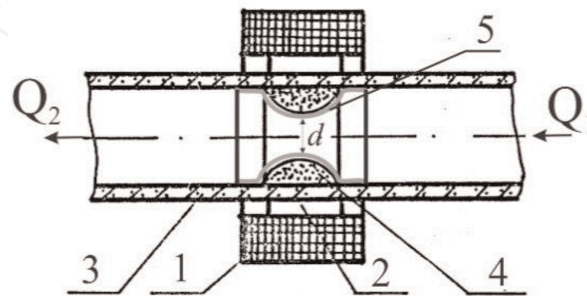


Figure 8.
 Micro choke structure containing magnetorheological fluid transmissions: 1—solenoid; 2—constant magnet; 3—tube; 4—magnetic fluid; 5—silicone; and Q_1 , Q_2 —working medium flow.

is being sheared. MR fluid is placed between two approaching plates and compressed, while magnetic field lines pass through the fluid in squeeze mode [31].

The MR fluid application in valve mode is presented in this research. Magnetorheological effect can be used in controlled choke structures which might be characterised as low power and pressure (see **Figure 8**).

This structure consists of the solenoid 1 with a constant magnet of ring shape 2 and bladder tube 3 coaxially fitted into its cylindrical opening. Tube 3 is filled with 4, which consists of the plug of toric segment shape in a silicone bag, along the constant magnet 2. Under choking, geometrical measures of MR fluid 4 plug and its magnetization force, which is being hold at the internal wall of bladder tube 3, depend on the gradient of magnetic field created by the constant magnet 2 and solenoid 1. If the solenoid 1 is powered by supply voltage from a control unit (no indication of it in the drawing), the field strength and the shape of free surface of MR fluid plug in a working gap change. The diameter d of the opening also changes under choking. Thus, it proceeds to the work medium flow regulation.

The substantiation of the mathematical model is based on the ferrohydrostatic equation [33, 34]:

$$\text{grad}p = \rho \bar{g} + \mu_0 M \text{grad}H \quad (26)$$

and the correlation of pressure capillary jump on a free surface

$$p = p_0 - \alpha(K_1 + K_2) \quad (27)$$

where K_1 and K_2 refer to the main curvatures of normal sections on a free surface, α refers to surface stress coefficient, p_0 refers to pressure of external environment, p refers to fluid pressure, ρ refers to density, g refers to free fall acceleration, μ_0 refers to vacuum magnetic penetration, $M = M(H)$ refers to fluid magnetization and H refers to magnetic field penetration.

First, let us deduce formulas of main curvatures of normal sections. Suppose

$$x = r(s) \cos \phi, \quad y = r(s) \sin \phi, \quad z = z(s) \quad (28)$$

It is known that main curvatures of normal sections on surfaces can be expressed through coefficients of the first and the second Gauss form as follows:

$$K_1 + K_2 = \frac{EN - 2FM + GL}{EG - F^2} \quad (29)$$

In this case

$$E = \left(\frac{\partial x}{\partial s}\right)^2 + \left(\frac{\partial y}{\partial s}\right)^2 + \left(\frac{\partial z}{\partial s}\right)^2 = r'^2 \cos^2 \phi + r'^2 \sin^2 \phi + z'^2 = r'^2 + z'^2 = 1, \quad (30)$$

$$F = \frac{\partial x}{\partial s} \frac{\partial x}{\partial \phi} + \frac{\partial y}{\partial s} \frac{\partial y}{\partial \phi} + \frac{\partial z}{\partial s} \frac{\partial z}{\partial \phi} = -r'^2 \cos^2 \phi \cdot r \sin \phi + r'^2 \sin^2 \phi \cdot r \cos \phi = 0 \quad (31)$$

$$G = \left(\frac{\partial x}{\partial s}\right)^2 + \left(\frac{\partial y}{\partial s}\right)^2 + \left(\frac{\partial z}{\partial s}\right)^2 = r'^2 \sin^2 \phi + r'^2 \cos^2 \phi = r'^2 \quad (32)$$

$$L = \frac{\bar{r}''_{S^2} (\bar{r}'_{S^x} \bar{r}'_{\phi})}{\sqrt{EG - F^2}} \quad (33)$$

$$N = \frac{\bar{r}''_{\phi^2} (\bar{r}'_{S^x} \bar{r}'_{\phi})}{\sqrt{EG - F^2}} \quad (34)$$

where

$$\bar{r}''_{S^2} = (r'' \cos \phi, r'' \sin \phi, z'') \quad \bar{r}'_{S^x} = (r' \cos \phi, r' \sin \phi) \quad (35)$$

$$\bar{r}'_{\phi} = (-r \sin \phi, r \cos \phi, 0) \quad \bar{r}''_{\phi^2} = (-r \cos \phi, -r \sin \phi, 0)$$

After integration of Eq. (26) according to z

$$r'' = -z' \left[\frac{\rho g z}{\vartheta} - \frac{\mu_0 M^* H^*}{\vartheta} \log \left(\frac{H^*}{H} \operatorname{sh} \frac{H}{H^*} \right) + C - \frac{z'}{r} \right] \quad (36)$$

When $s = 0$, there are following terms:

$$r(0) = R_0, \quad r'(0) = -\sin \alpha_0, \quad z'(0) = -\cos \alpha_0, \quad (37)$$

And when $s = s^*$,

$$z(s^*) = 0, \quad r'(s^*) = 0, \quad z'(s^*) = -1 \quad (38)$$

The task is solved in the non-symmetric form:

$$(\bar{r}z')' = \bar{r}r' \left[B_0 \frac{\bar{z}}{\bar{r}^2(0)} - A_1 \phi(\bar{r}, \bar{z}) + C \right] \quad (39)$$

The digital algorithm with non-inertial variables is investigated:

$$\frac{z_i^{n+1} - z_i^n}{\tau} = \frac{1}{r_i^n} \left(\frac{r_{i-1}^n + r_i^n}{2} z_{s,i}^{n+1} \right)_{s,i} - \frac{B_0}{(r_0^n)^2} \left[z_i^{n+1} (r_{s,i}^n)^+ + z_i^n (r_{s,i}^n)^- \right] + r_{s,i}^n [A_1 \phi(r_i^n, z_i^n) - C^n] \quad (40)$$

where $i = 1, \dots, N - 1$

$$z_{s,0}^{n+1} = -\frac{h}{2} \left[\frac{B_0}{(r_0^n)^2} z_i^{n+1} - A_1 \phi(r_i^n, z_i^n) - C^n + \frac{\cos \alpha_0}{r_0^2} \right] \sin \alpha_0 - \cos \alpha_0 \quad (41)$$

$$z_N^{n+1} = 0;$$

$$\frac{r_{i-1}^n + r_i^n}{\tau} = r_{s,i}^{n+1} + z_{s,i}^{n+1} \left[\frac{B_0}{(r_0^n)^2} z_i^{n+1} - A_1 \phi(r_i^n, z_i^n) - C^n - \frac{z_{s,i}^{n+1}}{r_i^n} \right] \quad (42)$$

There are two sets of items E_i^n and F_i^n such that for each set of elements, C is valid:

$$z_i^{n+1} = E_i^n z_{i+1}^{n+1} + F_i^n \quad (43)$$

After the analytical studies, the relationships are obtained:

$$z_i^{n+1} = \frac{A_i^n}{B_i^n - C_i^n E_{i-1}^n} z_{i+1}^{n+1} + \frac{D_i^n + C_i^n F_{i-1}^n}{B_i^n - C_i^n E_{i-1}^n} \quad (44)$$

and

$$E_i^n < \frac{A_1^n}{B_1^n - (1 + 2c_0 h^2) C_1^n} < \frac{A_1^n}{A_1^n + 1 - 2c_0 h^2 C_1^n} < 1 \quad (45)$$

Two sets of ε_i and V_i are determined:

$$r_i^{n+1} = \varepsilon_i r_{i+1}^{n+1} + v_i^n \quad (46)$$

where

$$\varepsilon_i = \frac{\alpha_i}{\beta_i - \gamma_i \varepsilon_{i-1}}, i > 1 \quad (47)$$

$$v_i^n = \frac{\vartheta_i^n + \gamma_i v_{i-1}^n}{\beta_i - \gamma_i \varepsilon_{i-1}}, i > 1 \quad (48)$$

After analytical study is found:

$$r_N^{i+1} = \frac{v_{N-1}^n}{1 - \varepsilon_{N-1}} \quad (49)$$

MR fluid magnetic field strength in a working gap has been measured, and the shape of MR fluid plug on free surface has been set [33].

In order to prevent the damage that might be done by pressure transmitted through the micro choke P_1 on the shape of MR fluid plug on free surface under choking, pressure P_1 should not reach the free surface magnetic field force, which has been created.

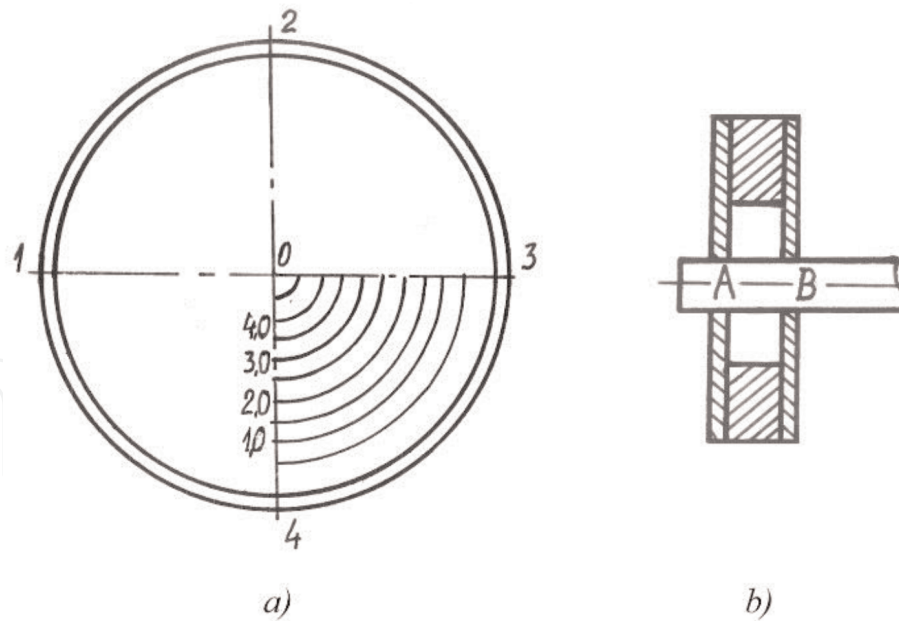


Figure 9. Scheme of the identifying magnetic field: (a) measuring directions 3–0 and 4–0; (b) measuring points A and B.

Distance from the outside of glass tube h , $\times 10^{-3}$ m	Magnetic field strength H , $\times 10^3$ A/m			
	Direction 4–0		Direction 3–0	
	Point A	Point B	Point A	Point B
0.5	46.871	44.006	47.587	49.179
1.0	36.526	35.651	31.672	34.139
1.5	31.911	24.112	25.942	29.682
2.0	24.987	20.611	19.178	19.417
2.5	20.451	16.870	20.531	15.120
3.0	16.313	10.425	14.801	10.504
3.5	12.812	5.730	11.539	7.639
4.0	11.459	1.751	10.504	4.138
4.5	6.287	1.035	4.218	1.592

Table 2. MR fluid magnetic field strength in a working gap of the micro choke.

Experiments allowed identifying [33] magnetic field strength at concentrators (points A and B, **Figure 9**) moving from the outside of glass tube to the centre in two perpendicular to each other directions, i.e. from point 4 to point 0 and from point 3 to point 0, in steps of 0.5×10^{-3} m. Research results are presented in **Table 2** and **Figure 10**.

3.2 Study of microcompressor with MR fluid

The operation principle of the microcompressor drive with MR liquid under study has been presented in paper [35]. **Figure 11** shows part of the general microprocessor view.

In the cylindrical system of axes, when the coordinate axis coincides with the rotor axis, the motion of viscous incompressible MR fluid vane is described by Navier-Stokes equations [36], which are expressed as follows:

$$-\frac{\partial p'}{\partial r'} + \frac{1}{Fr_m} \frac{\partial S'_m}{\partial r'} + \frac{R+r}{(R+1)^2} = 0 \quad (50)$$

$$-\frac{\partial p'}{\partial \varphi} + \frac{1}{Fr_m} \frac{\partial S'_m}{\partial \varphi} + \frac{\tau \delta (R+r')}{\rho u_0^2} = 0 \quad (51)$$

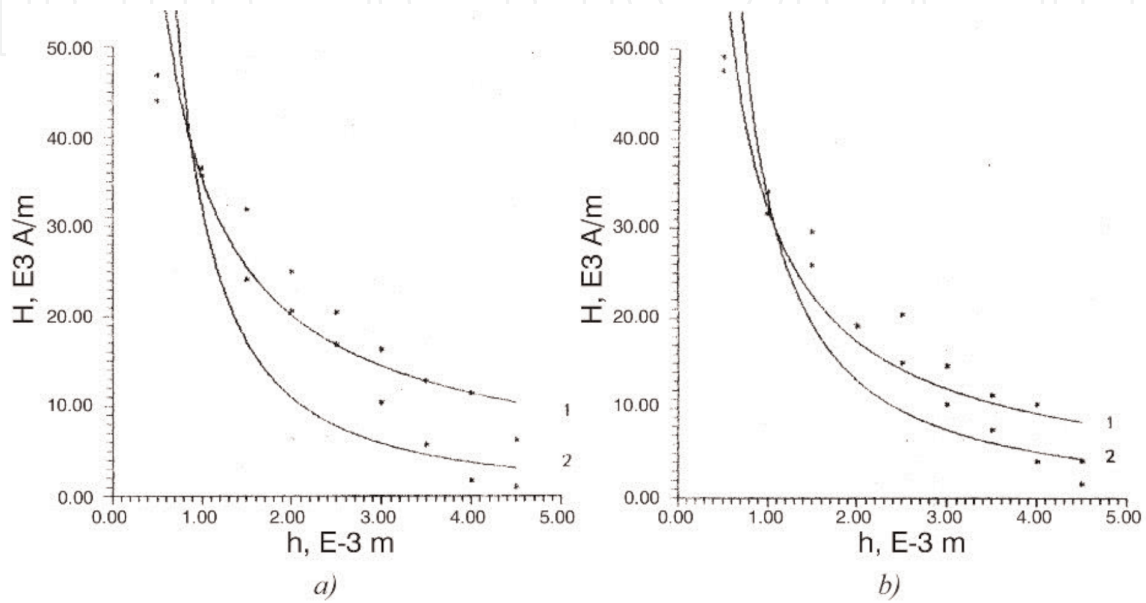


Figure 10. Correlation between the magnetic field strength H and the distance from a tube wall being measured in two directions: (a) 4–0, 1, measures taken at point A; 2, measures taken at point B; (b) 3–0, 1, measures taken at point A, and 2, measures taken at point B.

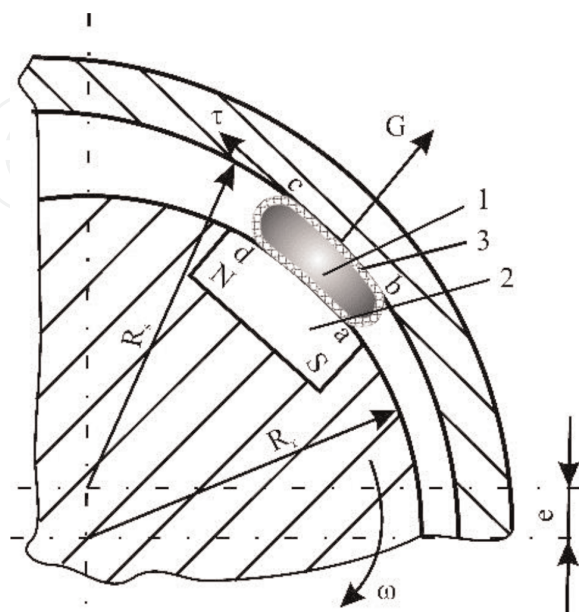


Figure 11. Scheme of an actuator with MR fluid: 1—MR fluid vane; 2—permanent magnet; 3—silicone shell; R_s —stator radius; R_r —rotor radius; e —eccentricity; a , b and c , d —free surface of MR fluid; G —centrifugal force; ω —rotor angular velocity; S and N —poles of permanent magnet; and τ , shear stresses.

where $Fr_m = \frac{\rho u_0^2}{\mu_0 M_s H_*}$ is magnetic Froude number; $S'_m = \ln \frac{sh \xi}{\xi}$ is a nondimensional coordinate function of the magnetic field; $r' = \frac{R+r_a}{R+1}$ is a nondimensional relative coordinate; ρ is the density of the magnetic fluid (kg/m^3); δ is the mean thickness of the working aperture between the rotor and the stator (m); u_0 is the vane velocity at the stator (m/s); μ_0 is magnetic permittivity (H/m); $M_s = \varphi_{dal} M_{s0}$ is magnetic saturation of the magnetic fluid (A/m); φ_{dal} is the number of particles in a volume unit; M_{s0} is magnetic saturation of a particle (A/m); $H_* = \frac{kT}{\mu_0 m}$ is the intensity of the magnetic field (A/m); k is Boltzmann constant; T is temperature (K); $m = V_{dal} M_{s0}$ is the magnetic moment of the particle; V_{dal} is the volume of the magnetic particle (m^3); $\xi = \frac{\mu_0 m H}{kT}$ is the argument of Langevin function, $\tau = (R + r')$ $\left[\frac{\partial^2 v}{\partial r'^2} + \frac{1}{(R+r')} \frac{\partial v}{\partial r'} - \frac{v}{(R+r')^2} \right]$; $v = u_0 v'$ is the azimuth component of velocity (m/s); and v' is nondimensional velocity.

When studying the efficiency of the drive, it is important to know MR fluid pressure upon the stator surface. When $r' = 1$, the vane pressure upon the stator surface is [35]

$$\begin{aligned}
 p' = p'_a + \frac{1}{Fr_m} [S'_m - S'_m(0, \varphi_a)] + \frac{1}{2} \left[\left(\frac{R+r'}{R+1} \right)^2 - \left(\frac{R}{R+1} \right)^2 \right] + \\
 + \frac{6(R+1)}{Re} (\varphi - \varphi_a) = \Sigma(r', \varphi) - \Sigma(0, \varphi_a) + p'_a
 \end{aligned} \quad (52)$$

The performed calculations have shown that the maximum pressure developed by the actuator reaches 10.8×10^3 Pa, when $n = 5000$ r/min, $q = 0.8$ and $\delta = 2 \times 10^{-3}$ m.

For experimental study of an actuator with MR fluid, a stand (Figure 12) was made with the following technical parameters: the internal diameter of the stator $D_s = 18 \times 10^{-3}$ m, the external diameter of the rotor $D_r = 15 \times 10^{-3}$ m, the rotor

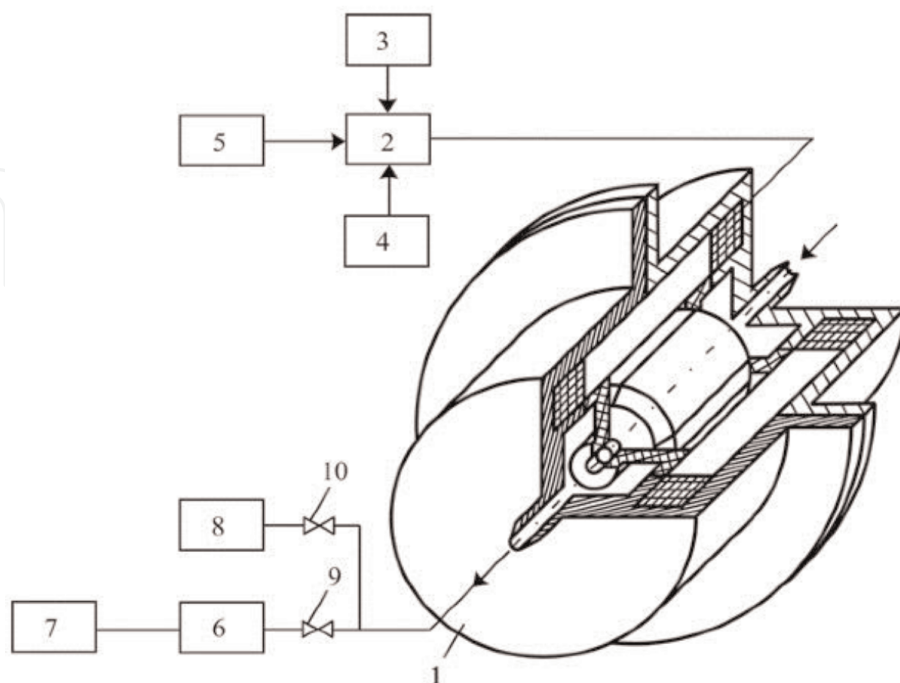


Figure 12. Scheme of an experimental stand for the actuator with MR liquid: 1—transducer; 2—control panel; 3, 4—power supply; 5—impulse generator; 6—diaphragm; 7—micromanometer; 8—telltale manometer; and 9, 10—valve.

working length $L = 8 \times 10^{-3}$ m, the eccentricity $e = 5 \times 10^{-5}$ m, the volume of the working chamber $V = 6 \times 10^{-7}$ m³, the number of permanent magnets is 4, the supply voltage $U = 15$ V, the supply current $I = 0.7$ A, the rotation frequency of the rotor $n = 0 \div 5000$ r/min, the MR fluid magnetic saturation $M_s = 51.7$ kA/m, the MR fluid density $\rho = 1585$ kg/m³ and the diameter of magnetic particles $R_{dal} = 9.01 \times 10^{-9}$ m [35].

The distribution of magnetic field in the working aperture of electromagnetic-magnetic systems with MR fluid determines the magnetic-hydrodynamic characteristics of the fluid. Therefore, the magnetic induction in the transducer's working aperture was measured with teslameter (by inserting a sensitive element with Hall sensor into the aperture). The measurements were made both at the surface of the rotor and the stator at 30°. The results of the measurements are presented in **Figure 13**. It has been determined that the highest value of magnetic induction is in the narrowest place of the working aperture at the rotor surface, reaching 0.745 T. The dissemination of magnetic induction at separate poles (magnet) does not exceed 1.2%. The experimental stand was also used for determining the values of the pressure and efficiency generated by the transducer. When the transducer rotor with the magnetic fluid vanes is rotating, the pressure difference developed in diaphragm is registered by micromanometer. According to the manometer readings, the pressure and the efficiency developed by the transducer are calculated.

The dependence of the pressure generated by the transducer on the MR fluid vane-filling coefficient while changing the rotation frequency is shown in **Figure 14**.

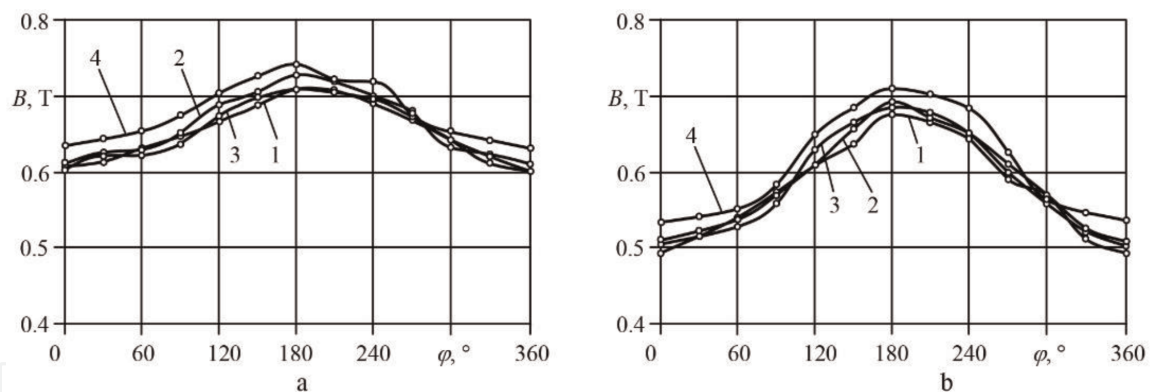


Figure 13. Dependence of magnetic induction in working aperture upon the rotor turn angle: (a) at the rotor surface; (b) at the stator surface; 1—first magnet; 2—second magnet; 3—third magnet; and 4—fourth magnet.

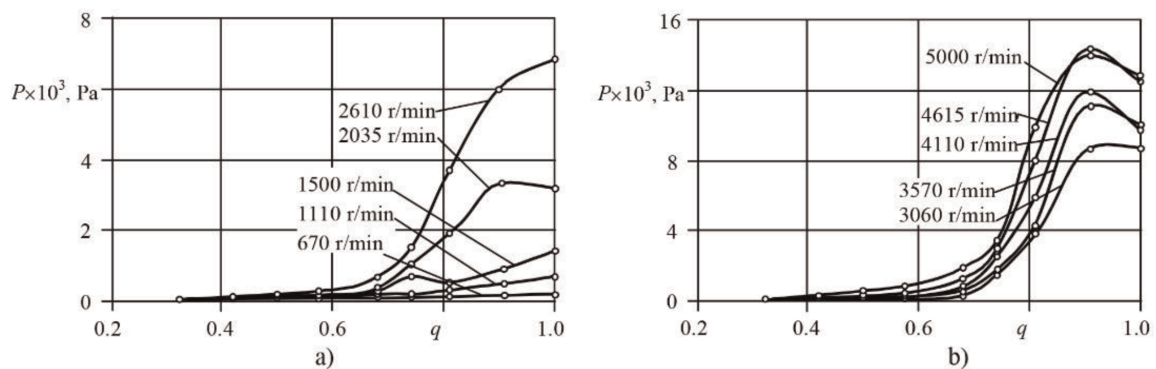


Figure 14. Dependence of pressure p generated by the transducer upon the MR fluid vane-filling coefficient while changing the rotor rotation frequency: (a) frequency changed from 670 to 2610 r/min; (b) from 3060 to 5000 r/min.

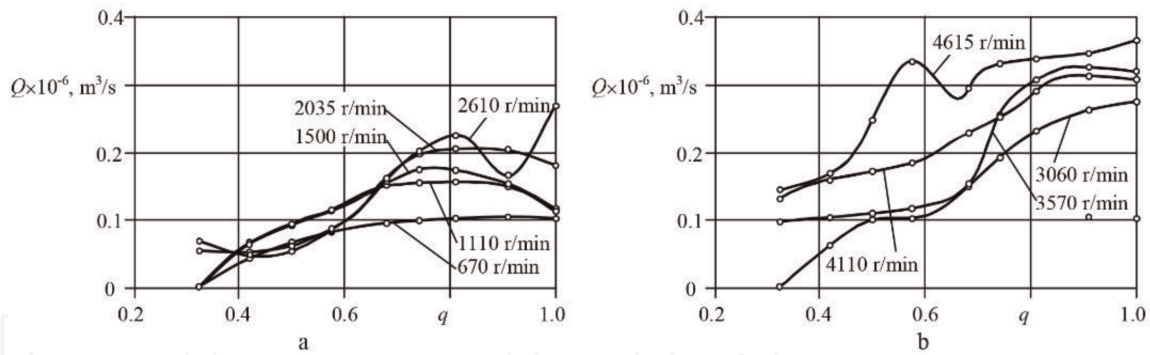


Figure 15.

Dependence of efficiency developed by the transducer upon MR fluid vane-filling coefficient q , when changing the rotor rotation frequency n : (a) frequency changed from 670 to 2610 r/min; (b) from 3060 to 4615 r/min.

As seen from the presented charts, the value of the pressure generated by the actuator depends directly on the MR fluid vane-filling coefficient and the rotation frequency. The highest pressure value is obtained when MR fluid-filling coefficient is close to 0.9. The generated pressure increases with increasing rotation frequency (up to 13.7 kPa, when $n = 4615$ r/min). **Figure 15** shows the dependence of the transducer's efficiency upon MR fluid vane-filling coefficient while changing the rotation frequency of the rotor.

The study results show that the transducer's capacity also depends on the rotation frequency of the rotor and MR fluid vane-filling coefficient. However, only at low rotation frequencies of the rotor (up to 2000 r/min), the capacity rises gradually with changing MR fluid vane-filling coefficient. The maximum value of the efficiency achieved is $0.37 \times 10^{-6} \text{ m}^3/\text{s}$.

4. Conclusions

4.1 The performed study of the shape memory elements in pneumatic actuators leads to the following conclusions

The numerical researches have showed dependence of the maximal displacement of middle point of bended plate when both plate's ends are fastened, on the reaction stresses. A numerical methodology has been proposed which describes the changeable volume of chamber with smart material element.

The presented engineering methodology enables to determine dependence of force generated by plate with shape memory material on mechanical stresses.

The theoretical research has shown that the change of chamber volume affects the parameters of auto vibrations in vibroexciter. During the studies of the plate of the titanium-nickel alloy TN-1, it was estimated that maximum deformation of plate, whose length $l = 25 \times 10^{-3} \text{ m}$, height $h = 1.5 \times 10^{-3} \text{ m}$ and width $b = 20 \times 10^{-3} \text{ m}$, changed the volume of chamber in vibroexciter by 7.5%. It caused an amplitude of vibrations to decrease in 9.1% and frequency to increase in 0.7%. Other SM alloys which have different characteristics and better deformation properties in the direction of Y axis can be used in the construction of vibroexciters. In some technological processes for precise vibroexciters, a minor change of the frequency is also important.

The methodology of calculations used in present research evaluates the deformation of the plate only approximately. For more precise calculations, it is necessary to evaluate the temperature deformations, cross stress and the fact that part of

the deformation energy is transferred to the heat used to replace the material structure.

The obtained study results may be applied in designing equipment, containing SMA elements.

4.2 The performed study of the transducer with MR fluid leads to the following conclusions

The value of the pressure generated by the transducer actuator depends directly on MR fluid vane-filling coefficient and rotation frequency. The highest pressure value is obtained when MR fluid-filling coefficient is close to 0.9. The pressure increases with increasing rotation frequency (up to 13.7 kPa, when $n = 4615$ r/min).

The efficiency developed by the transducer also depends on the rotation frequency of the rotor and on MR fluid vane-filling coefficient. The maximum obtained efficiency value is $0.37 \times 10^{-6} \text{ m}^3/\text{s}$.

At low MR fluid vane-filling coefficient q values—up to 0.67—unstable work areas of the transducer caused by hermetic flaws of the system have been observed.

Findings of theoretical and experimental studies are sufficiently adequate; the obtained pressure values do not exceed 15%.

Further studies are needed to ensure hermetic properties of the system with MR fluid vanes.

Thanks

The authors thank Prof. Habil and Dr. Ramutis Bansevicius for the ideas and help in the theoretical research and experiments.


IntechOpen

Author details

Edmundas Kibirkštis*, Darius Pauliukaitis and Kęstutis Vaitasius
Faculty of Mechanical Engineering and Design, Kaunas University of Technology,
Lithuania

*Address all correspondence to: edmundas.kibirkstis@ktu.lt

IntechOpen

© 2019 The Author(s). Licensee IntechOpen. This chapter is distributed under the terms of the Creative Commons Attribution License (<http://creativecommons.org/licenses/by/3.0>), which permits unrestricted use, distribution, and reproduction in any medium, provided the original work is properly cited. 

References

- [1] Kibirkštis E et al. Synchronization of pneumatic vibroexciters on air-cushion operating under self-exciting autovibration regime. *Journal of Mechanical Science and Technology*. 2017;**31**(9):1-8
- [2] Pauliukaitis D, Kibirkštis E. Application of smart materials in structural elements of pneumatic vibroexciters. In: *Solid State Phenomena*. Zurich, Switzerland: Trans Tech Publications; 2017. pp. 40-44
- [3] Stupelis L, Kibirkštis E, Liaudinskas R, Dabkevičius A. Engineering calculation methods of SM element deformation. In: *ACTUATOR 2000, 7th International Conference on New Actuators*; 19–21 June, 2000; Bremen, Germany; 2000
- [4] Ding X, Kuribayashi K, Hashida T. Development of new micro gas valve composed of a SMA thin film and micro distance sensor. In: *ACTUATOR 2000, 7th International Conference on New Actuators*; 19–21 June, 2000; Bremen, Germany; 2000
- [5] Hafez M, Khelfaoui F, Nesnas H, Chaillet N. Monolithic SMA large surface with a high-density of micro actuators for tactile displays. In: *ACTUATOR 2004, 9th International Conference on New Actuators*; 14–16 June, 2004; Bremen, Germany; 2004
- [6] Jia H, Lalande F, Rogers CA. Modeling of strain energy absorption in superelastic shape memory alloys. In: *Smart Structures and Materials 1997: Mathematics and Control in Smart Structures*. San Diego, California: International Society for Optics and Photonics; 1997. pp. 548-559
- [7] Liaudinskas R, Baurienė G, Kibirkštis E, Vaitasius K. Study of Pneumatic Damper with Transducers made from Materials with Shape Memory. *Mokslinių tyrimų rinkinys - Mechanika Nr. 3(10)*. Kaunas, Lithuania: KTU, Technologija; 1997. pp. 46-49
- [8] Cisse C, Zaki W, Zineb TB. A review of constitutive models and modeling techniques for shape memory alloys. *International Journal of Plasticity*. 2016; **76**:244-284
- [9] Dutta SC, Majumder R. Shape memory alloy (SMA) as a potential damper in structural vibration control. In: *Advances in Manufacturing Engineering and Materials*. Cham: Springer; 2019. pp. 485-492
- [10] Gao Y et al. An origin of functional fatigue of shape memory alloys. *Acta Materialia*. 2017;**126**:389-400
- [11] Frenzel J et al. On the effect of alloy composition on martensite start temperatures and latent heats in Ni–Ti-based shape memory alloys. *Acta Materialia*. 2015;**90**:213-231
- [12] Savi MA et al. Shape memory alloys. In: *Dynamics of Smart Systems and Structures*. Cham: Springer; 2016. pp. 155-188
- [13] Humbeeck J, Reynnaerts D, Stalmaus R. Shape memory alloys: Functional and Smart. In: *4th International Conference on New Actuators—ACTUATOR'94, Konferencija*; Bremen, Vokietija; 1994. *Pranešimų Medžiaga*; Bremen: AXON Technologie Consult GmbH; 1994. pp. 312-316
- [14] Hesselbach J, Stork H. Simulation and control of shape memory actuators. In: *Proceedings of 5th International Conference on New Actuators – ACTUATOR 96; Konferencija*; Bremen, Vokietija. *Pranešimų medžiaga*; Bremen: AXON

Technologie Consult GmbH; 1996.
pp. 369-399

[15] Villafana A, Masse M, Portier R, Pons J. Thermomechanical testing machine conceived for the study of shape memory alloys. Application to the training and testing of the two-way memory effect. In: IVth European Symposium on Martensitic Transformations; Journal de Physique IV Colloque; France; 1997. pp. 655-660

[16] Mertmann M, Hornbogen E. Grippers for the micro assembly containing shape memory actuators and sensors. In: IVth European Symposium on Martensitic Transformations; Journal de Physique IV Colloque; France; 1997. pp. 621-626

[17] Patoor E et al. Shape memory alloys. Part I: General properties and modeling of single crystals. *Mechanics of Materials*. 2006;**38**(5-6):391-429

[18] Pauliukaitis D, Kibirkštis E, Ragulskis K. Problems of precise vibromechanics and vibroengineering. *Vibroengineering Procedia*. 2016;**8**: 377-385

[19] Bewerse C, Brinson LC, Dunand DC. Microstructure and mechanical properties of as-cast quasibinary NiTi-Nb eutectic alloy. *Materials Science and Engineering A*. 2015;**627**:360-368

[20] Brinson LC. One-dimensional constitutive behavior of shape memory alloys: Thermomechanical derivation with non-constant material functions and redefined martensite internal variable. *Journal of Intelligent Material Systems and Structures*. 1993;**4**:229-242

[21] Hao T. *Electrorheological Fluids: The Non-Aqueous Suspensions*. Amsterdam, The Netherlands: Elsevier; 2011. p. 578. ISBN: 0080455441

[22] Choi SB, Han YM. *Magnetorheological Fluid Technology:*

Applications in Vehicle Systems. Boca Raton: Taylor & Francis; 2012. p. 310. ISBN: 1439856737

[23] Martin Laun H, Kormann C, Willenbacher N. *Rheometry on Magnetorheological (MR) Fluids*. Rheola Acta: Steinkopff Verlag; 1996. pp. 417-420

[24] Carlson JD. Magnetorheological fluids. In: Schwartz M, editor. *Smart Materials*. USA: CRC Press/Taylor & Francis Group; 2009. pp. 17.1-17.6

[25] Ghaffari A, Hashemabadi SH, Ashtiani M. A review on the simulation and modeling of magnetorheological fluids. *Journal of Intelligent Material Systems and Structures*. 2015;**26**(8): 881-904

[26] Fonseca HA et al. Magnetic effect in viscosity of magnetorheological fluids. *Journal of Physics: Conference Series*. IOP Publishing. 2016;**687**(1):012102

[27] Kordonski W, Gorodkin S. The behavior of a magnetorheological (MR) fluid under compressive deformation. *Journal of Rheology*. 2016;**60**(1):129-139

[28] Ruiz-López JA et al. Simulations of model magnetorheological fluids in squeeze flow mode. *Journal of Rheology*. 2017;**61**(5):871-881

[29] Xu F-H et al. A compact experimentally validated model of magnetorheological fluids. *Journal of Vibration and Acoustics*. 2016;**138**(1): 011017

[30] Rossi A et al. A review on parametric dynamic models of magnetorheological dampers and their characterization methods. *Actuators*. 2018;**7**(2):16

[31] Farjoud A et al. Nonlinear modeling and testing of magneto-rheological fluids in low shear rate squeezing flows.

Smart Materials and Structures. 2011;
20(8):085013

[32] Conrad H, Sprecher AF.
Characteristics and mechanisms of
electrorheological fluids. *Journal of
Statistical Physics*. 1991;**64**(5–6):
1073-1091

[33] Kibirkštis E, Vaitasius K.
Investigation of actuators with smart
links. *Journal of Vibroengineering*.
2008;**10**(1):98-103

[34] Stupelis L. An initial boundary-
value problem for a system of equations
of magnetohydrodynamics. *Lithuanian
Mathematical Journal*. 2000;**40**(2):
176-196

[35] Kibirkštis E, Vaitasius K,
Pauliukaitis D. Investigation of
actuators with magnetorheological
liquid. In: *Mechanika 2006: Proceedings
of the 11th International Conference;*
April 6–7, 2006; Lithuania: Kaunas
University of Technology/Kaunas
University of Technology, Lithuanian
Academy of Science, IFTOMM National
Committee of Lithuania, Baltic
Association of Mechanical Engineering;
2006

[36] Stupelis L. *Navier-Stokes Equations
in Irregular Domains*. Amsterdam, The
Netherlands: Springer Science &
Business Media; 2013